Recent increase in surface melting of West Antarctic ice shelves linked to Interdecadal Pacific Oscillation

Check for updates

Pranab Deb [1] ✉, David Bromwich [2], Andrew Orr[3], Arnab Sen [1] & Kyle R. Clem [4]

Since the late 1990s, summer surface melt across ice shelves in the Ross-Amundsen Sea sector of West Antarctica increased significantly, as demonstrated by satellite measurements and MetUM simulations. This contrasts with the period from 1979 to the late 1990s, which witnessed a decreasing summer melt trend driven by the positive trend in Southern Annular Mode. The increase in summer melt since the late 1990s is linked to an increase in geopotential height and intensified anticyclonic blocking along coastal West Antarctica, which strengthened northerly winds over the Ross-Amundsen Sea sector, leading to enhanced advection of warm, marine air. Our analysis reveals a strong connection between summer melt indices and sea surface temperatures in the South Pacific Convergence Zone during this period. Moreover, increased summer precipitation in South Pacific Convergence Zone since the late 1990s strengthened the Rossby wave teleconnection toward West Antarctica, contributing to enhanced blocking along the coastal region. This is consistent with the transition of the Interdecadal Pacific Oscillation to its negative phase.

Recent studies have highlighted the prevalence of surface meltwater over the ice shelves and coastal margins of West Antarctica (WA), particularly during austral summer[1–3]. The ponding, movement, and drainage of the surface meltwater may cause the ice shelves to flexure and/or hydrofracture[4–8], which in some cases could trigger their collapse[9]. The thinning and collapse of ice shelves diminishes their buttressing effect on tributary glaciers, accelerating the flow of glacier ice into the ocean and contributing to sea level rise[10–13]. Higher levels of atmospheric warming in the coming decades will likely intensify summer surface melting over the WA ice shelves[14,15], raising the risk of ice shelf disintegration in this region. This, in turn, could lead to the dynamic destabilization and/or retreat of the WA ice sheet, further accelerating grounded ice loss and contributing to sea level rise[16,17].

Melting of a snow/ice surface occurs when the near-surface air temperatures reach the melting point 273.15 K[3]. Because of the tight coupling between surface melt and near-surface air temperatures, near-surface air temperature is often used as a proxy for the occurrence of surface melt[3]. Surface melting over Antarctic ice shelves can be caused by a number of processes, including heat advection, vertical turbulent mixing of sensible heat[18], or radiative forcing[14,19–21]. These processes are tied to both regional scale events such as foehn winds, katabatic winds, and barrier winds[3], as well as changes to the regional atmospheric circulation[3,22]. In particular,

Scott et al.[23] reported an increase in summer melt-duration over ice shelves in the Ross-Amundsen Sea sector of WA since the late 1990s due to increased advection of warmer marine air over this region, as well as reduced sea ice cover in the Ross–Amundsen Seas, which was associated with intense blocking activity in the Amundsen Sea region.

Remote influences from tropical Pacific Ocean sea surface temperature (SSTs) variability can strongly modulate the regional circulation and climate of WA by influencing the location and strength of the ASL[3,21–24]. These influences notably include the El Niño - Southern Oscillation (ENSO)[25], as well as variability in SSTs over the South Pacific Convergence Zone (SPCZ) region[3], which can influence the climate of WA on interannual timescales[3,21–24]. Other remote influences shown to influence the WA climate on decadal and longer timescales include low-frequency modes of climate variability such as the Pacific Decadal Oscillation, Interdecadal Pacific Oscillation (IPO) and the Atlantic Multidecadal Oscillation[26–30]. Significantly, the shift of the IPO to its negative phase in the late 1990s was associated with warming over the Ross Ice Shelf and sea ice expansion in the Ross Sea region[21,28], as well as cooling over the Antarctic Peninsula[31]. However, the impact of this IPO phase transition on melt trends over WA ice shelves remains unknown, presenting a significant knowledge gap. Moreover, while both the eastern Pacific Ocean[28] and the SPCZ[32] have been proposed as key source areas for the IPO teleconnection to WA,

[1]Centre for Ocean, River, Atmosphere and Land Sciences (CORAL), Indian Institute of Technology Kharagpur, Kharagpur, India. [2]Polar Meteorology Group, Byrd Polar and Climate Research Center, The Ohio State University, Columbus, OH, USA. [3]British Antarctic Survey, Cambridge, United Kingdom. [4]School of Geography, Environment and Earth Sciences, Victoria University of Wellington, Wellington, New Zealand. ✉e-mail: pranab@coral.iitkgp.ac.in
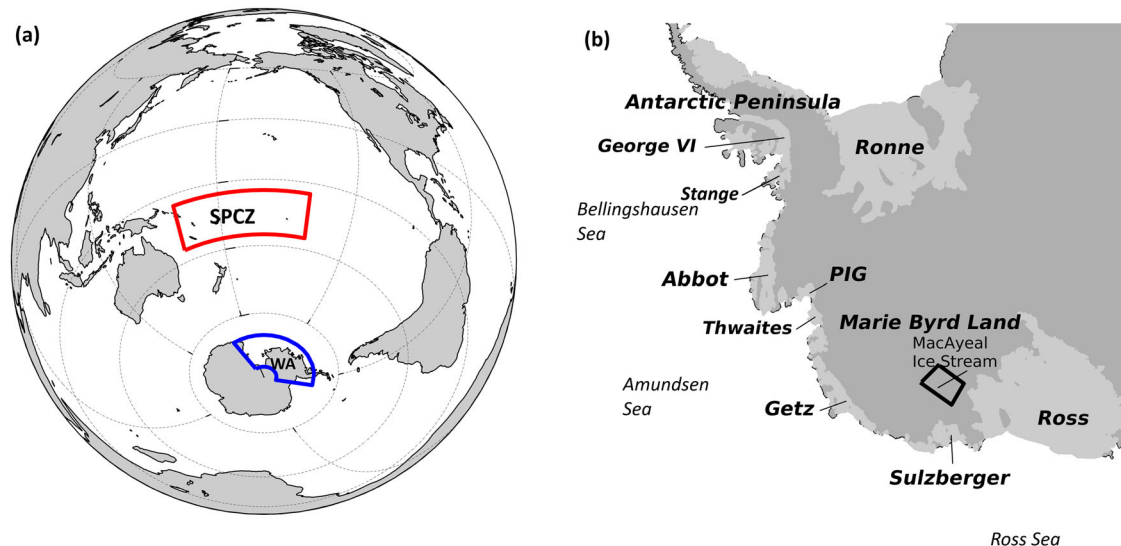
Fig. 1 | Depiction of the study domain. a Pacific Ocean sector of the Southern hemisphere. The red and blue boxes show the geographical extent of the South Pacific Convergence Zone (SPCZ) and West Antarctica (WA), respectively, as used in this study. **b** West Antarctic domain, including key ice shelves and geographic locations referenced in the study. The black rectangle shows the geographical extent of the MacAyeal Ice Stream region used in the stacked anomaly calculation.

uncertainties remain regarding which region predominantly controls the regional circulation and cryospheric changes in the region. Further, the mechanisms through which IPO-induced precipitation changes in the SPCZ influence blocking activities in the Amundsen Sea region are yet to be resolved.

In this study, we investigate the impact of IPO's transition to its negative phase in the late 1990s on the summer melt trends across WA ice shelves. We further explore the mechanistic link between convective activities in the SPCZ, Amundsen Sea blocking events and surface melt in the region. Figure 1 shows the locations of the ice shelves discussed in this study, as well as other key regions.

Results and discussion
Summer surface melt trends over WA
Figure 2 shows maps of linear trends of the number of melt days over WA observed by passive microwave satellite measurements (n_{mlt}) from 1979 to 1998 and 1998 to 2018, which are hereafter referred to as period-1 and period-2, respectively. These results are broadly similar to those reported by Scott et al.[23], and show that the majority of ice shelves situated in the Ross-Amundsen Sea sector of WA exhibited a negative trend in n_{mlt} during period-1 (Fig. 2a), which reversed to a significant positive trend during period-2 (Fig. 2c). During period-2, the positive trends in n_{mlt} extend as far eastwards as the western sector of the Abbot ice shelf, with the largest positive trends over the Getz ice shelf, Sulzberger ice shelf, and the eastern flank of the Ross ice shelf including the MacAyeal ice stream region (refer to Fig. 1b for ice shelf locations).

To further investigate these summer melt trends, we also examine an air temperature-based metric of potential melt based on outputs from a regional atmospheric model (MetUM)[3]. Here, we use the frequency component of the melt potential, defined as the frequency of daily summer maximum near-surface temperatures exceeding a melt threshold of 273.15 K, referred to as "melt potential frequency" (MP_f). In the Ross-Amundsen sea sector, areas exhibiting a reversal of n_{mlt} trends over the two periods also show a reversal in MP_f trends (Fig. 2b, d), i.e., signifying an increase in the frequency of daily maximum air temperatures exceeding the melt threshold during period-2, which is consistent with the increase in the number of melt days. In contrast, the ice shelves in the Bellingshausen Sea region of WA exhibited opposite trends, characterized by positive trends in both n_{mlt} and MP_f during period-1, followed by negative trends during period-2, although the significant

trends are confined primarily to Stange and George VI ice shelves. Note that over the eastern Ross Ice Shelf, the distribution of significant trends is scattered and lacks a homogeneous spatial pattern. In contrast, the Abbot Ice Shelf is characterized by an absence of significant trends. Notably, the western part of the Abbot Ice Shelf shows weak positive trends in both periods that are statistically insignificant, suggesting that this area likely represents a transition zone for the dipole shift in melt trends across WA.

Furthermore, we derived stacked time series of the n_{mlt} and MP_f melt metrics from 1979 to 2018 for the Ross-Amundsen Sea sector by averaging the normalized anomalies for each metric extracted from the Getz and Sulzberger ice shelves, the eastern sector of the Ross ice shelf, and the MacAyeal ice stream region (Supplementary Fig. 1). This confirms the contrasting melt trends between period-1 and period-2, and the significant upward trend over this region since the late 1990s. Also, the application of the sequential Mann–Kendall test[31] confirms that the observed trend reversal over this region is statistically robust. The results from our trend analysis are also independent of the trend change point which was confirmed by shifting the change point by +/- 3 seasons[23]. This effectively removes the influence of the 1998–2000 triple dip La Niña following the strong El Niño episode in 1997/98.

Role of regional atmospheric circulation
The analysis of geopotential height at 500 hPa (z500) and meridional wind at 850 hPa (v850) over Antarctica and the surrounding Southern Ocean reveals distinct trends between period-1 and period-2 (Fig. 3). During period-1, a negative trend in z500 over the continent and an annular belt of positive trend in z500 over the Southern Ocean forms a pattern resembling the positive southern annular mode (SAM). This is consistent with the significant positive SAM trend (0.15 year^{-1}, $p < 0.05$) observed during this period. A significant negative correlation ($r = -0.5$, $p < 0.05$) between SAM and the "stacked" surface melt anomaly in the Ross-Amundsen Sea sector further supports that the positive SAM trend played a key role in reducing melt in the region during period-1. The positive SAM trend is expected to intensify the ASL[33–35], as indicated by the negative trend in z500 over the Ross-Amundsen Sea region (Fig. 3a). This drives a positive trend in v850 over the Ross-Amundsen Sea sector of WA (Fig. 3c), strengthening the southerly winds and reducing the advection of warm air, which explains the decrease in surface melt in the Ross-Amundsen Sea sector during period-1 (Fig. 2a, b). However, the v850 trend along the Ross-Amundsen coast is
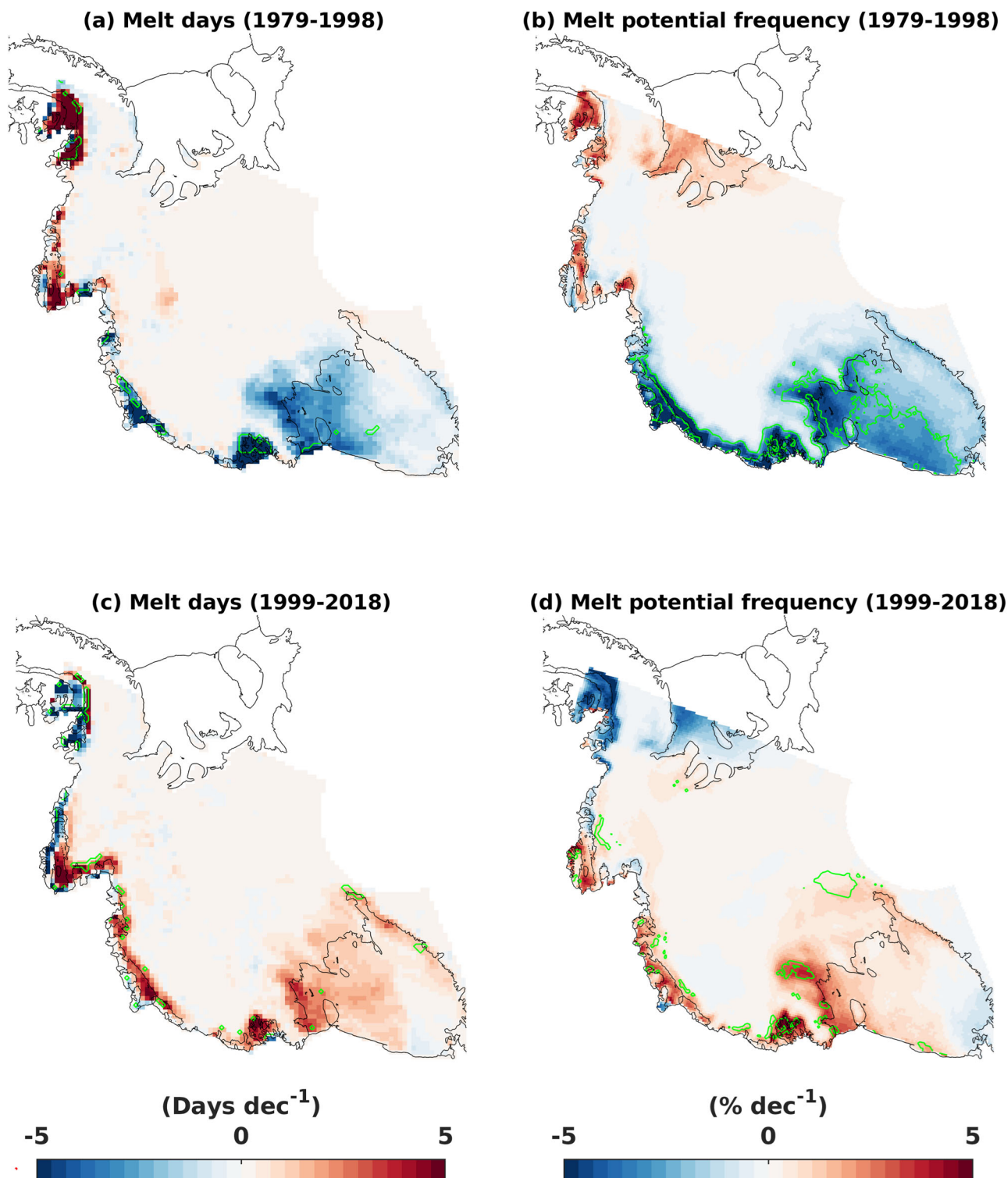
Fig. 2 | Decadal trends in melt indices over coastal West Antarctica. Trends in (left column, **a, c**) melt days (n_{mlt}) based on passive microwave satellite measurements, and (right column, **b, d**) melt potential frequency (MP$_f$) based on regional atmospheric model output, during (top panel) austral summer from 1979 to 1998 and (bottom panel) austral summer from 1999 to 2018. Areas with statistically significant trends (at 90% level) are shown with green contours.

insignificant, likely due to the high atmospheric variability in the WA region, often referred to as the "pole of variability[36]."

In contrast, during period-2, the trends in z500 show a distinctive east-west dipole across the Antarctic Peninsula, with positive trends over the Amundsen-Bellingshausen Sea region and a negative trend over the Weddell Sea region (Fig. 3b). The increasing trend in z500 over the Amundsen-Bellingshausen Sea region is consistent with the observed positive trend in

the Amundsen Sea blocking index (ASBI), and hence an increasing trend in the intensity of anticyclonic blocking events, during this period[23] (Supplementary Fig. 2). This suggests that the episodic advection of northerly air masses, driven by anticyclonic blocking over the Amundsen Sea region, is a key mechanism driving surface melt in the coastal Ross-Amundsen Sea region during period-2. To further examine the role of anticyclonic blocking events on melt trends during period-2, we calculated the correlation between
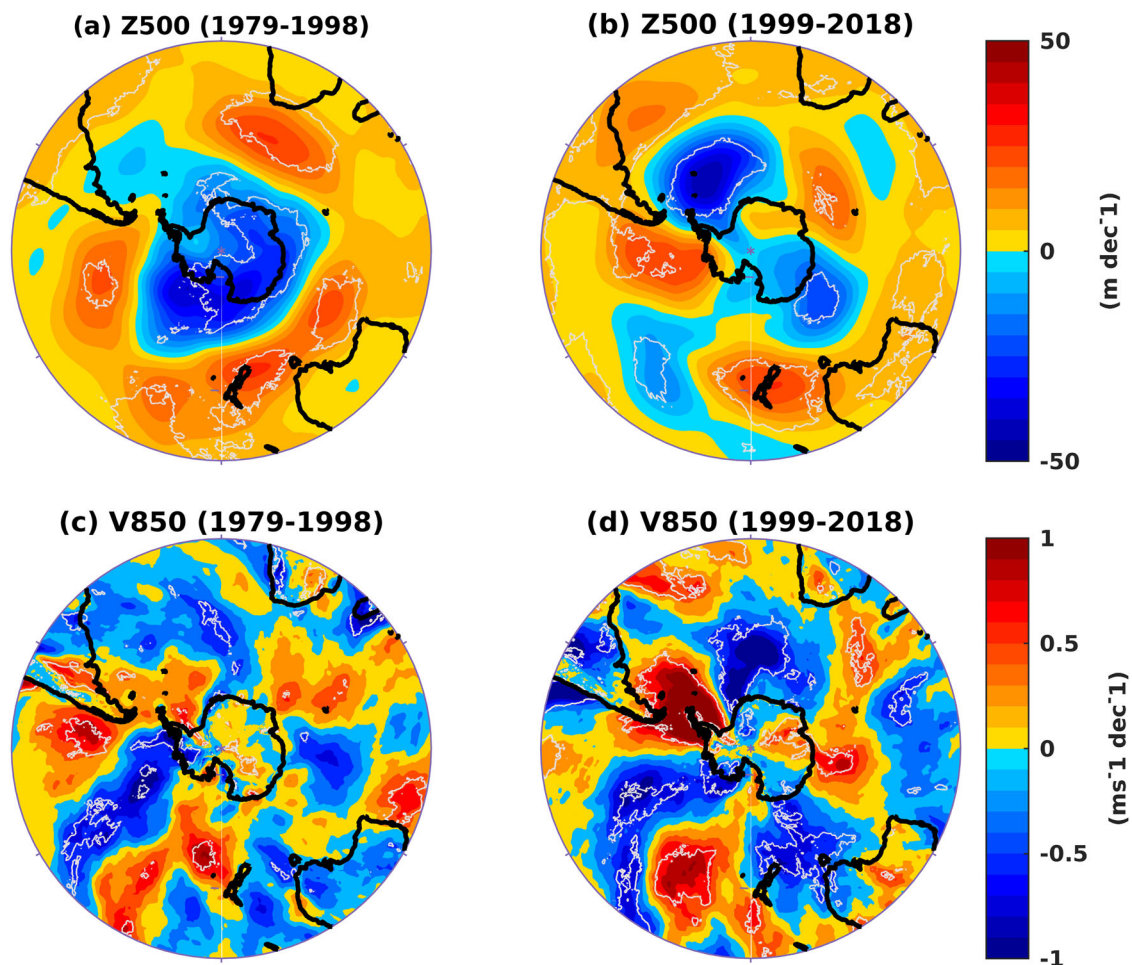
Fig. 3 | Decadal trends in z500 and v850 over coastal West Antarctica. Trends in (top panel, **a**, **b**) geopotential height at 500 hPa (m dec^{-1}) and (bottom panel, **c**, **d**) meridional wind at 850 hPa (ms^{-1} dec^{-1}), from ERA5 reanalysis, during austral summer of (left column) 1979–1998 and (right column) 1999–2018. Areas with significant trends (at 90% level) are shown with white contours.

the ASBI and the summer 'stacked' surface melt anomaly (derived from passive microwave satellite data) over the Ross-Amundsen Sea sector. Our analysis reveals a strong positive correlation ($r = 0.62$, $p < 0.01$) during period-2. Additionally, a strong negative correlation ($r = -0.86$, $p < 0.01$) was observed between ASBI and the area-averaged v850 anomaly over the coastal Ross-Amundsen Sea sector (encompassing the region 200-260°E, 55-70°S). Therefore, the increasing trend in anticyclonic blocking over the Amundsen Sea region, along with the associated increase in warm northerly air mass advection (v850) over the Ross-Amundsen Sea sector of WA (Fig. 3d), explains the positive melt trend over this region since the late 1990s (Fig. 2c, d). Notably, neither SAM nor ASL showed a significant correlation with melt in this region in period-2, suggesting their minimal influence during this period.

The positive trend in z500 over the Amundsen-Bellingshausen Sea and in the ASBI since the late 1990s aligns with the increase in the frequency of atmospheric rivers making landfall within the WA region since the early 21st century[37]. However, it is important to note that not all atmospheric river events lead to melting, and not all melt events are due to atmospheric rivers[38]. Interestingly, the positive z500 trend is also consistent with the increase in southerly flow over the eastern sector of WA, which is associated with the decreasing trend in melt during period-2 (Fig. 2c, d).

Role of SPCZ in driving the trend reversal in WA surface melting
The large-scale circulation trends in period-2 are markedly different from period-1, with the trends during period-2 being highly asymmetric and more reminiscent of a large-scale Rossby wave than SAM (Fig. 3). Here,

we investigate the role of the SPCZ in driving these distinct trends in large-scale circulation, which caused the shift in surface melting trends across coastal WA during austral summer from period-1 to period-2. In particular, we report shifts/differences in the correlation between area-averaged summer SSTs over the SPCZ region (encompassing the area of 5°-25°S and 160°–220°E, referred to as the "SPCZ box" hereafter) and n_{mlt} and MP$_f$ between the two periods (Fig. 4). In period-1, the correlation between SST over the SPCZ box and n_{mlt} and MP$_f$ over the coastal Ross-Amundsen Sea sector of WA is relatively weak (magnitude less than 0.35), characterized by predominantly insignificant and negative correlation values (Fig. 4a, c) (although a portion of the Ross ice shelf exhibits a significant negative correlation between SPCZ SST and MP$_f$ (Fig. 4c)). However, since the trends in melt days and MP$_f$ during period-1 over this region are well explained by a positive SAM pattern and associated strengthening of the ASL (Fig. 3), the influence of SPCZ SST during this period is of secondary importance.

In contrast, during period-2, there is a switch to a positive correlation between SST over the SPCZ box and n_{mlt} and MP$_f$ over the Ross-Amundsen Sea sector of WA, as well as parts of the Bellingshausen Sea sector of WA (Fig. 4b, d). Interestingly, the correlation between SPCZ SST and the ASBI also shows a significant increase in period-2, with a correlation value of 0.5 ($p < 0.05$) during this period, compared to an insignificant correlation in period-1. This suggests a strengthening of the SPCZ teleconnection to WA during summer in period-2, leading to a substantial influence on the ASBI and, consequently, on surface melting across the coastal Ross-Amundsen Sea sector.
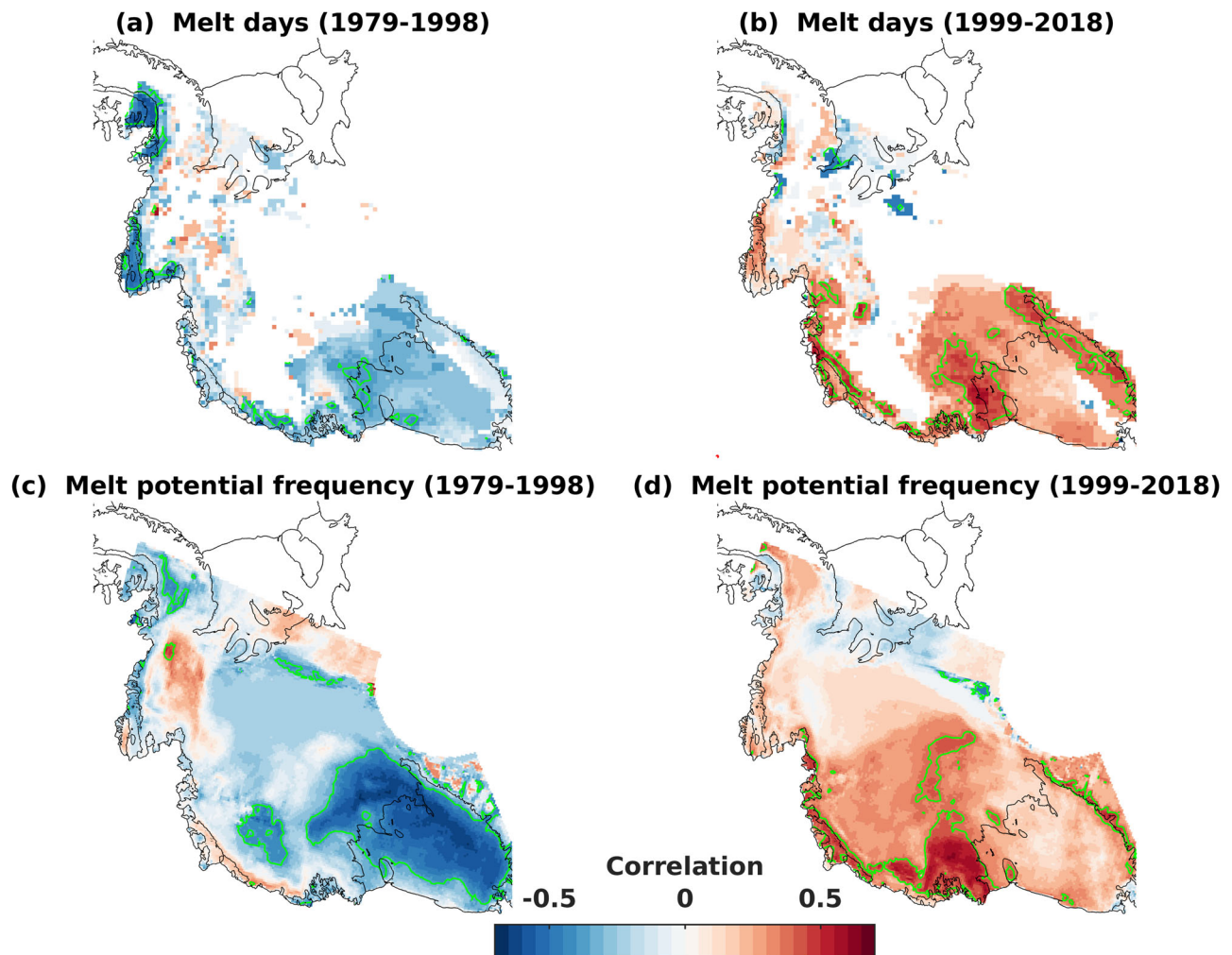
(a) Melt days (1979-1998)

(b) Melt days (1999-2018)

(c) Melt potential frequency (1979-1998)

(d) Melt potential frequency (1999-2018)

Correlation

-0.5   0   0.5

Fig. 4 | Correlation between SST over the SPCZ and melt indices over coastal West Antarctica. Correlation between area-averaged sea surface temperature in the SPCZ box and (top panel, **a, b**) melt days (n_{mlt}) based on passive microwave satellite measurement, and (bottom panel, **c, d**) melt potential frequency (MP_f) based on regional atmospheric model output over West Antarctica, during austral summer of (left, **a, c**) 1979–1998 and (right, **b, d**) 1999–2018. Statistically significant trends (at 90% level) are indicated by green contours. All time series were detrended prior to computing the correlations.

A strengthening of the SPCZ teleconnection is consistent with a significant increase in summer SST between period-2 and period-1 over the SPCZ box (Fig. 5a), which is accompanied by an increase in precipitation over the poleward edge of the box (Fig. 5b). These changes contrast with reduced SST and precipitation between these two periods in the tropical central-eastern Pacific Ocean (Fig. 5a, b). The increase in SST and precipitation over the SPCZ box is consistent with the impact of IPO on SST and precipitation variability along the southwest/poleward edge of the SPCZ[39], demonstrated here using regression maps of SST and precipitation onto the "residual" Tripole IPO Index (TPI) during austral summer (Fig. 5c, d). The shift in summer SST and precipitation patterns over the SPCZ box, and the broader Pacific Ocean, between period-2 and period-1 aligns with a shift in the phase of the IPO from positive to negative since the late 1990s[28,30,32,39]. We hypothesize that this shift since the late 1990s induces an enhanced extratropical Rossby wave response that serves as the primary component of the IPO teleconnection to WA during period-2.

Previous studies[40–43] have demonstrated that the extratropical Rossby wave response to anomalous convection in tropical and subtropical regions typically develops into a quasi-stationary wave pattern in the extratropics within 15–25 days. Therefore, it is crucial to use daily datasets to analyse the impact of SPCZ convection on atmospheric variability and anticyclonic blocking events in WA. We use the following approach to investigate the relationship: (a) calculate the daily ASBI using daily z500 anomalies, (b)

identify days where the index is in the upper quartile for both period-1 and period-2, and (c) compute the composite differences in daily SPCZ precipitation and outgoing longwave radiation (OLR), averaged over the 40 days preceding these upper-quartile blocking events, between period-2 and period-1 (Fig. 6). In period-2, the upper-quartile blocking events are associated with significantly ($p < 0.01$) higher SPCZ precipitation (>2 mm/day) and reduced OLR (<10 W/m²), compared to period-1, suggesting that the enhanced WA blocking events in period-2 are linked to enhanced convective activities in the SPCZ. Notably, the spatial pattern of enhanced convective activity within SPCZ preceding the WA blocking events (Fig. 6) closely resembles the pattern of enhanced precipitation during period-2, particularly in regions of significant increase (Fig. 5b). This suggests that the increasing trend in WA blocking events, and consequently the increase in surface melt since the late 1990s, is tied to intensified convection over SPCZ and is strongly associated with the IPO phase shift that occurred during this period.

Dynamics of SPCZ teleconnection to WA
Here, we examine the underlying dynamics of the SPCZ teleconnection to WA and its evolution since the late 1990s. We employ the linear response theory model (LRTM)[41–43] to quantify the extratropical Rossby wave response due to anomalous convection over the SPCZ box during the two periods. We force the LRTM with the area-averaged precipitation anomaly
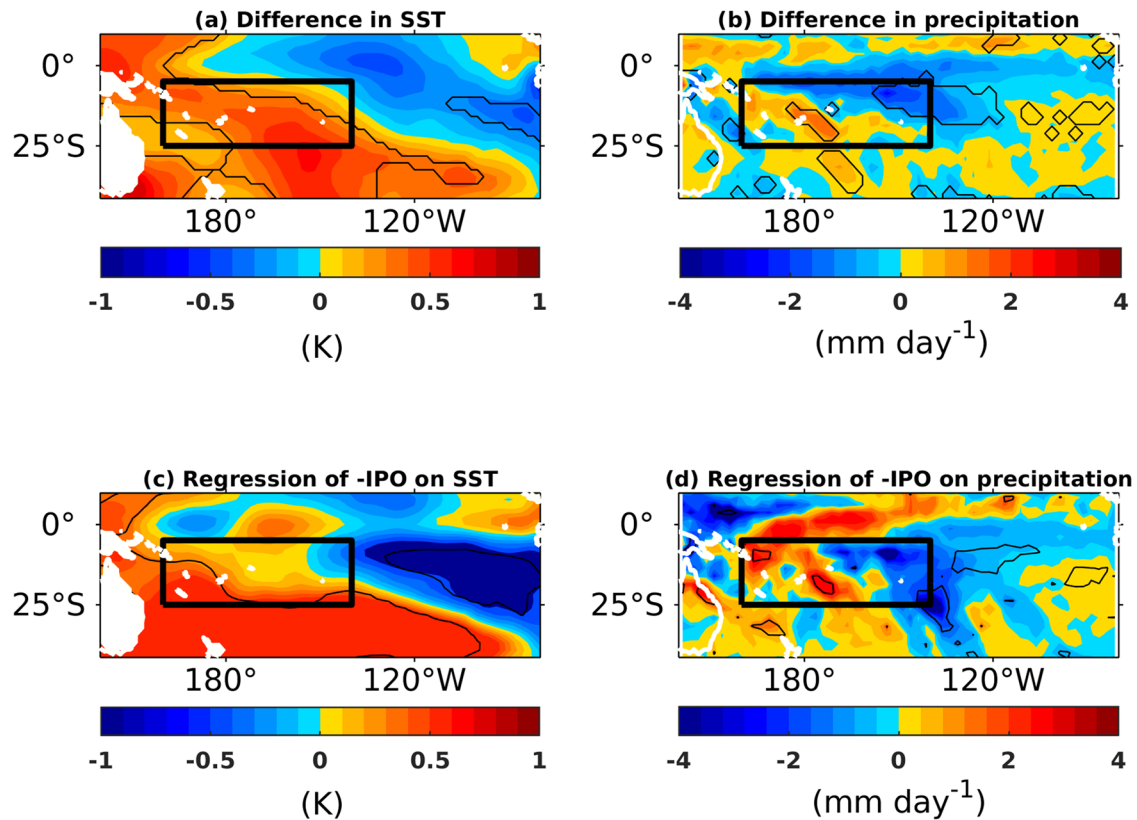
Fig. 5 | Changes in SST and precipitation over the SPCZ associated with IPO phase shift in the late 1990s. Maps showing differences of **a** sea surface temperature (K), and **b** precipitation (mm day^{-1}) over subtropical Pacific Ocean between period-2 (1999–2018) and period-1 (1979–1998) during austral summer (DJF). Maps showing the regression of residual IPO tripolar index onto **c** sea surface temperature and **d** precipitation (regression values are multiplied by (-1) for clarity). The black rectangle outlines the 'SPCZ box'. Black contours outline areas where the difference and regression values are significant at a 90% level.
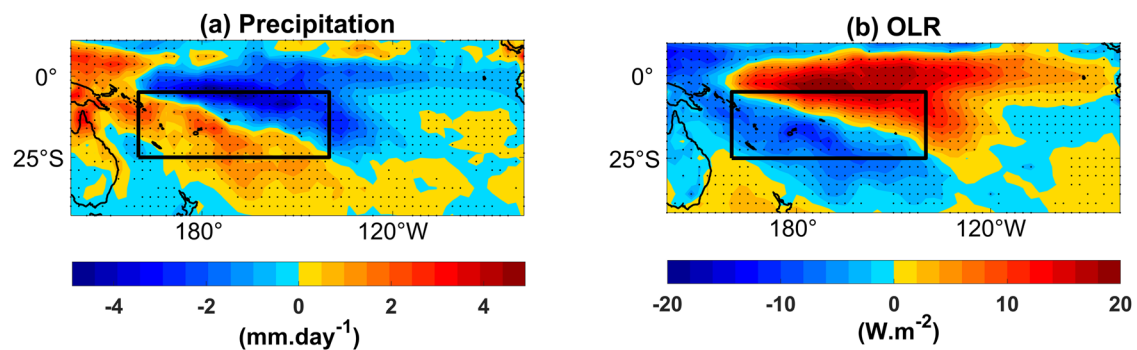

Fig. 6 | Relationship between SPCZ convection and atmospheric blocking events over coastal West Antarctica. Composite differences between period-2 and period-1 in (**a**) daily precipitation and (**b**) daily OLR, averaged over the preceding 40 days of the upper-quartile blocking events. The black dots outline areas where the differences are significant at a 99% level. The thick black rectangle outlines the "SPCZ box".

over the SPCZ box and record the cumulative response in the Southern Hemisphere geopotential height anomalies at 200 hPa (z200), during period-1 and period-2 (Fig. 7a, b). We selected z200 over z500 because the Rossby wave source is generated at the upper levels of the atmosphere, and the extratropical Rossby wave response is "equivalent barotropic". In period-1, the step response in the WA sector is comparatively weak and consists primarily of a positive geopotential height anomaly over the Ross-Amundsen Sea (Fig. 7a). This pattern is substantially different from the observed negative z500 trend (Fig. 3), suggesting that the observed trend during period-1 is not forced by SPCZ convection. In contrast, during period-2, the step response shows a distinctive east-west dipole (Fig. 7b), with a positive anomaly (i.e., anticyclonic blocking high) over the Amundsen-Bellingshausen Sea region, and a negative anomaly over the

Weddell Sea region. This pattern closely resembles the observed z500 trend during period-2 (Fig. 3). Further, the wave activity flux[44], computed using the step response in z200 anomalies from the LRTM, shows strong eastward and poleward Rossby wave propagation originating from the SPCZ region during period-2 (Fig. 7d). No discernible poleward wave propagation is apparent during period-1 (Fig. 7c). These results align closely with an earlier study which demonstrated that enhanced convection over the SPCZ can trigger an extratropical Rossby wave response, leading to anomalous high pressure over the Amundsen-Bellingshausen Sea in summer[32]. However, it is important to acknowledge that on interannual timescales, other circulation patterns, such as ENSO and SAM can dominate over the SPCZ teleconnection. But this does not diminish the significance of the SPCZ teleconnection as a major driver of long-term melt trends over WA.
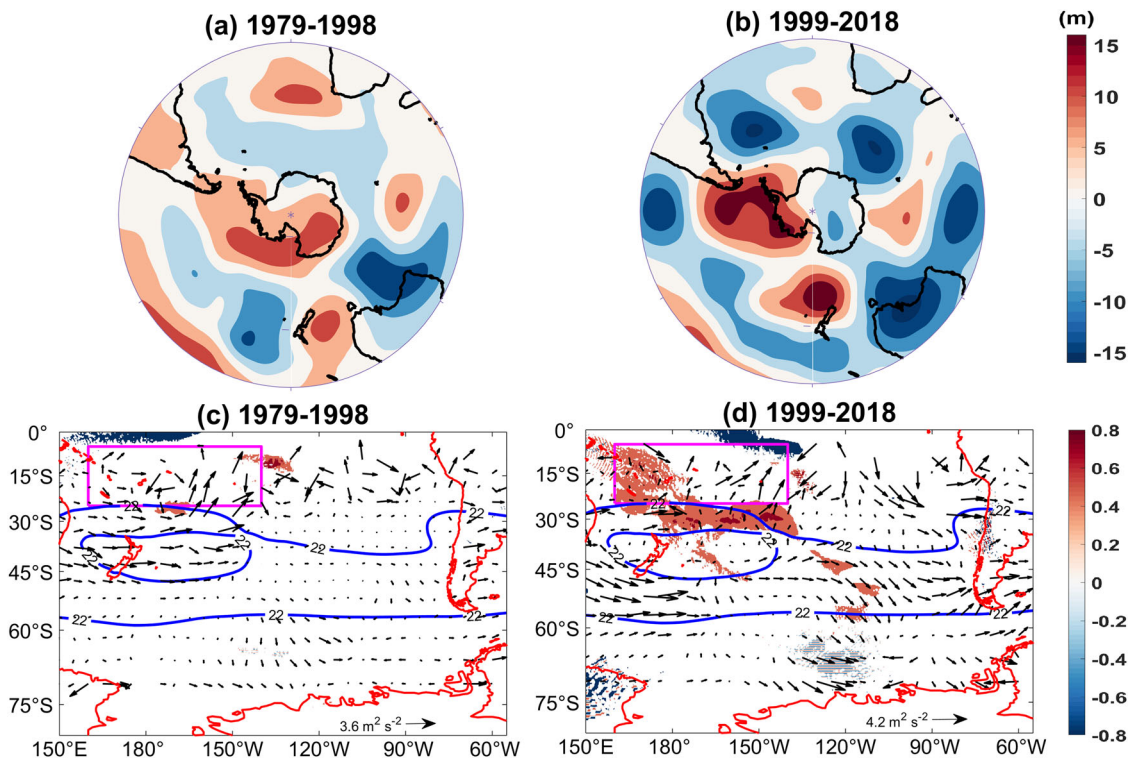
Fig. 7 | Extratropical response to SPCZ precipitation and associated Rossby wave source and waveflux activity. Step response function (computed from the "linear response theory model") for anomalous 200-hPa geopotential height (m), forced by an area-averaged precipitation anomaly over the SPCZ box, during austral summer of (**a**) 1979–1998 and (**b**) 1999–2018. The correlation between the Rossby wave source anomaly induced by the vorticity advection term and the area-averaged precipitation over the SPCZ box for the austral summer of (**c**) 1979–1998 and (**d**) 1999–2018 (shaded, values below 99% confidence interval are masked). Wave activity flux vectors (vectors, in $m^2 s^{-2}$) computed from the step response function during the austral summer of (**c**) 1979–1998 and (**d**) 1999–2018 are overlaid. Thick blue lines show the westerly jet (contours of 22 ms^{-1} zonal wind). The SPCZ is marked by a magenta box.

Convection within the SPCZ region is associated with an upper-level anomalous vorticity source and a climatological Rossby wave source (RWS) in the vicinity[32,45]. The RWS consists of two components, which are the vortex stretching term and the advection of the mean absolute vorticity by the anomalous divergent flow[45,46]. The vortex stretching term represents the impact of vertical stretching or compression of air columns on vorticity, where divergence increases cyclonic vorticity (and downstream trough development), and convergence increases anticyclonic vorticity (and downstream ridge building). The vorticity advection term describes vorticity transport by the irrotational wind associated with divergent flow, which generates Rossby waves by vorticity advection and associated geopotential height changes as explained by the quasi-geostrophic height tendency equation. We computed the correlation between the area-averaged SPCZ precipitation anomaly and the two components of the RWS anomaly for period-1 and period-2. The correlation against the vortex stretching term in both periods is weak (Supplementary Fig. 3). This is consistent with earlier findings that the vortex stretching term may not necessarily be an effective RWS in some cases, particularly over strong divergent regions in the subtropics[45,46]. However, during period-2, SPCZ precipitation is positively correlated with the vorticity advection term immediately to the south of the SPCZ box (Fig. 7d). This is in line with earlier findings from a perturbation experiment (Supplementary Fig. 2a of Clem et al.[32]) which showed that the RWS in the vicinity of SPCZ region is enhanced in response to anomalous precipitation anomaly over the SPCZ region. The stronger SPCZ convection since the late 1990s results in increased upper-level divergent flow (Supplementary Fig. 3d) which, together with the upper-tropospheric vorticity gradient of the subtropical jet stream, results in a stronger RWS near the southern boundary of the SPCZ region (primarily due to the increased advection of the mean absolute vorticity by the anomalous divergent flow). This sets the stage for a strong and robust Rossby wave teleconnection to the

Ross-Amundsen Sea sector of WA, forced by the SPCZ region, since the late 1990s. It is important to note that an equal and opposite response is not seen in period-1 when SPCZ convection was suppressed. This is likely due to the localized nature of SPCZ forcing, the teleconnection is active only during the period of active/enhanced convection (i.e., in period-2). This contrasts with large-scale patterns (e.g., ENSO) which are associated with approximately equal and opposite teleconnection patterns during the contrasting phases due to large-scale changes in overturning circulations. This difference arises from the persistence of active convection in both ENSO phases, but with a flip in the spatial pattern and a shift in the region of convective forcing between the phases.

Finally, to assess the impact of teleconnections from tropical regions other than the SPCZ on WA surface melt, we analysed the difference in precipitation between period-2 and period-1 during summer across the tropics (Fig. 8a). We identified eight tropical regions (excluding the SPCZ, highlighted by magenta boxes in Fig. 8a) that experienced a significant increase in precipitation during period-2. For each of these regions, we conducted separate experiments using the LRTM, applying area-averaged DJF precipitation anomalies as forcing and calculating the step responses in the 200-hPa geopotential height anomalies. The resulting step responses (Fig. 8b–i) differed significantly from the observed z500 trend during period-2, and none reproduced the positive geopotential height anomaly over coastal WA. This indicates that the observed WA circulation changes during period-2 are primarily driven by teleconnections from the SPCZ, not from other tropical regions.

Conclusion
Overall, based on analysis spanning the period from 1979 through 2018, we provide evidence that the increasing summer melt trend observed since the late 1990s across the major ice shelves in the Ross-Amundsen Sea sector of
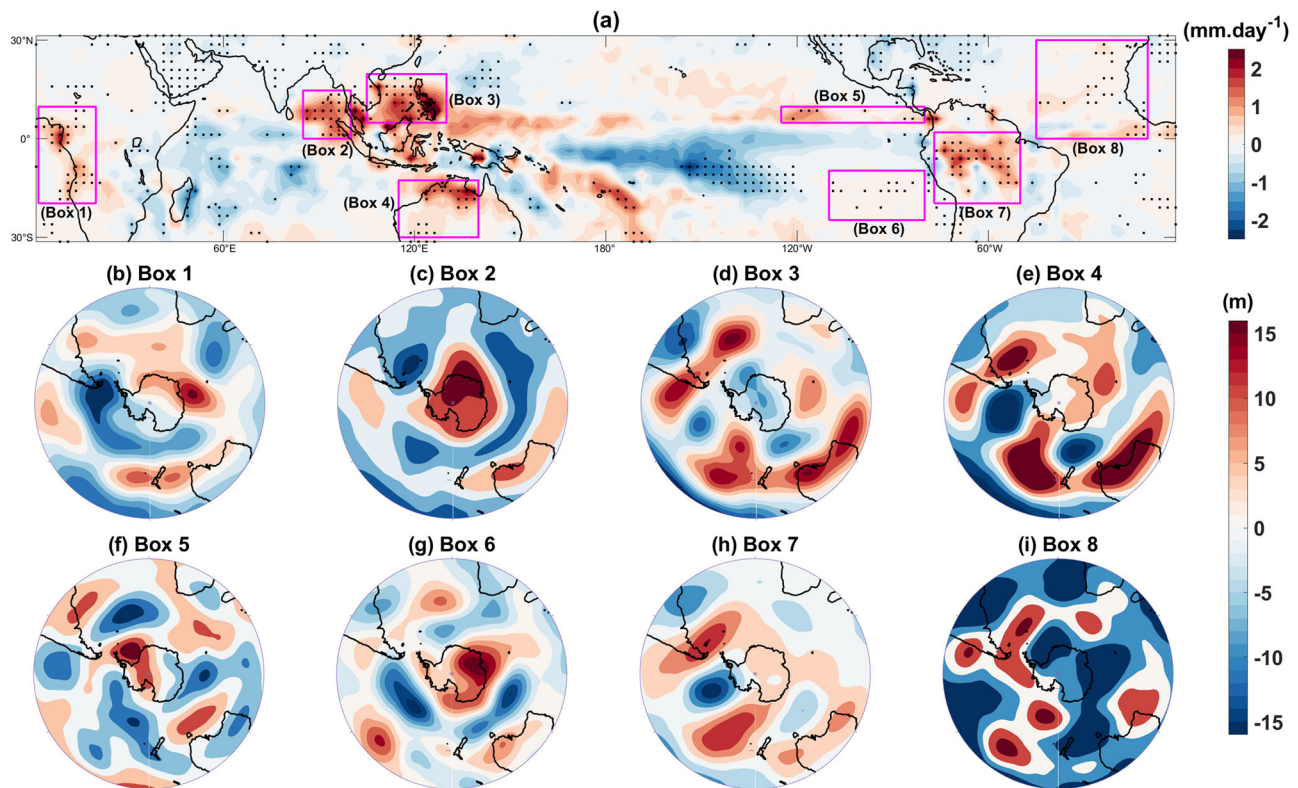
Fig. 8 | Extratropical response to precipitation anomalies at selected tropical regions. a Map showing a difference of precipitation over the tropics between period-2 (1999–2018) and period-1 (1979–1998) during austral summer (DJF). Difference values significant at the 90% level are dotted. Regions with positive precipitation changes (except SPCZ region), used to compute the step responses are marked by magenta boxes. **b–i** Step response function (computed from the "linear response theory model") for anomalous 200-hPa geopotential height, forced by area-averaged precipitation anomaly over eight boxes shown in figure (**a**), during austral summer of 1999–2018.

WA is primarily driven by an increasing trend in z500, and the associated intensification of anticyclonic blocking, over the Amundsen-Bellingshausen Sea region. Furthermore, we demonstrate that these changes are driven by enhanced SST and convective activity in the SPCZ, concurrent with the transition of the IPO to its negative phase since the late 1990s.

Interestingly, sea ice expansion in the Ross Sea sector since the late 1990s (statistically significant only in the austral autumn season) was previously reported to be driven primarily by the cooling observed in the equatorial eastern Pacific, consistent with the negative phase of the IPO[28]. However, cooling in the equatorial eastern Pacific fails to reproduce the observed trend in regional circulation during the summer months (Fig. 3a of Meehl et al.[28]). Consequently, while convective anomalies over the equatorial eastern Pacific may hold importance for other seasons, the IPO teleconnection to WA during the austral summer is primarily dominated by the influence of the SPCZ. Similarly, a trend reversal was noted in surface air temperature over the Antarctic Peninsula in the late 1990s, concurrent with the IPO phase shift, with a significant cooling trend in austral summer during 1999–2014[31]. This cooling trend since the late 1990s is consistent with passive microwave satellite observations showing reduced melting on the eastern part of WA (Fig. 2c), and along the east side of the Antarctic Peninsula extending to the Larsen Ice Shelf[23]. The cooling trend was primarily attributed to the cyclonic conditions in the northern Weddell Sea (extended data Fig. 4a of Turner et al.[31]). Our analysis shows that the cyclonic conditions over the Weddell Sea since the late 1990s is likely a part of the SPCZ teleconnection to WA. It is imperative to consider these trend reversals associated with IPO phase change when detecting and attributing climate change across coastal WA.

Finally, the impact of natural variability in the Pacific is superimposed on a long-term background cooling over most of Antarctica driven by a positive SAM trend in summer[47–51]. This is corroborated by the weak decreasing trend in melt indices over the major ice shelves in WA during DJF 1979–2018 (Supplementary Fig. 4)[2,3]. The significant negative trends are concentrated over the eastern sector of WA which is consistent with the deepening of ASL. The summer melt trends across coastal WA in the upcoming decades will depend on the shift in the IPO phase as well as on how the SAM responds to the recovery of the Antarctic ozone hole and greenhouse forcing.

Methods

Satellite observations

The surface melt data utilized in this study can be accessed and retrieved from the following website: https://snow.univ-grenoble-alpes.fr/melting/. This is based on passive microwave radiometer data obtained from the SMMR (scanning multichannel microwave radiometer) platform prior to July 1, 1987, and the SSM/I (special sensor microwave/imager) platforms thereafter. The dataset provided has a spatial resolution of 25 km. The dataset offers daily measurements with a temporal resolution of 1 day, except for the period prior to 1988 where measurements are only available every 2 days. It spans a nearly continuous period from 1979, excluding a data gap during the summer of 1987/1988. The algorithm developed by Torinesi et al.[52] and Picard and Fily[53] is employed to derive surface melting information from the passive microwave radiometer data. For each pixel and day, the dataset includes the classification of wet or dry snow conditions. The pixel classification is as follows: 0 represents dry snow, 1 indicates wet snow, and −10 represents unavailable data or masked regions. The data is provided on a stereographic polar grid with a resolution of 25×25 km². In Antarctica, a cropped version of the Southern stereographic polar grid employed by National Snow and Ice Data Center (NSIDC) is utilized. The dataset excludes ocean areas and regions above 1700 m.a.s.l. The mask remains constant over time, which poses considerations in cases where the coastline has changed during the time series.

Regional atmospheric model

The atmospheric model employed in this study is the Met Office Unified Model version 11.1 (MetUM), utilizing the Global Atmosphere 6.0 configuration suitable for regional applications at grid scales of 10 km or coarser. The model is run over the standard Antarctic CORDEX domain, employing a grid spacing of 0.11° (~12 km) with a grid size of 392 × 504 points, as well as 70 vertical levels up to a height of 80 km. It covers the period from December 1979 to February 2019, encompassing 40 summer (December-February) melt seasons. The ERA-Interim reanalysis data is used to force the model. The MetUM's high spatial resolution facilitates a more accurate depiction of localized processes that impact surface melting on ice shelves[3], as well as ensuring comprehensive coverage of smaller ice shelves. The MetUM utilizes a frequent reinitialization method to generate hindcasts. This approach involves conducting twice-daily 24-h forecasts, specifically at 0000 and 1200 UTC. The outputs obtained at T + 12, T + 15, T + 18, and T + 21 h from each forecast are then combined to create a continuous series of 3-h model outputs. For further details regarding the model setup and approach, refer to Orr et al.[3].

Determination of surface melt and "melt-potential"

The number of melt days from passive microwave-base satellite measurements (n_{mlt}) corresponds to the count of days associated with surface melt, as identified by the satellite-based melt classification[52,53]. Further, we use output from the MetUM simulation to calculate the temperature-based melt potential frequency (MP_f)[3]. The MP_f assesses the likelihood of surface melting occurrence. At each grid point, a probability distribution function (PDF) of the daily temperature maxima is constructed. The area under the PDF corresponding to temperatures exceeding the melt threshold of 273.15 K is then calculated, quantifying the potential for surface melting to occur[3]. The austral summer season (December-January-February or DJF) considered in this study is December-centric, i.e., DJF of the year 1979 consists of December month of the year 1979 and January-February months of the year 1980.

Stacked anomaly time series of melt for the coastal Ross–Amundsen Sea sector

We computed a seasonal mean stacked anomaly time series of each of the three melt metrics (viz., n_{mlt} and MP_f) by averaging the normalized anomalies (anomalies are calculated relative to the full study period, i.e., 1979–2018) from Getz and Sulzberger ice shelves, the eastern sector of the Ross ice shelf (encompassing 150–165°W, 77–82°S), and the MacAyeal Ice Stream region (encompassing 139–147°W, 79–81°S). Use of a stacked anomaly time series for the coastal Ross–Amundsen Sea region is justified because of the strong similarity among the individual time series, and also because they are tied to the regional atmospheric circulation in a similar way[3].

Approximate trend turning points in the stacked anomaly time series of the different melt indices are detected using the sequential Mann–Kendall test[54]. Before applying the sequential Mann–Kendall test, contributions from ENSO and other variabilities with periods shorter than 10 years are removed from the stacked anomaly time series by using a low-pass Butterworth filter with a cut-off period of 11 years. Note that the sequential Mann–Kendall test provides an approximation of the timing of trend changes, often detecting multiple changes within a couple of years. More details of the sequential Mann–Kendall test can be found in Turner et al.[31].

Amundsen Sea blocking index

Following Scott et al.[23], the Amundsen Sea blocking index (ASBI) was computed from the standardized area-weighted mean of 500-hPa geopotential height anomaly over the region 50^0-70^0S and 230^0-280^0E.

Statistical tests

We use linear least squares for computing trend and regression and evaluate the significance of the trend using the Mann–Kendall test for linear monotonic trends. The significance of regression is assessed using a two-

tailed *t*-test. The significance of differences between the two periods is evaluated using a two-tailed *t*-test, while Satterthwaite's approximation is used for calculating the effective degrees of freedom (df: 38.6506).

Geographic boundaries

Satellite-based maps, collected as part of the Earth system data records for use in research environments (MEaSUREs) program during 2007–2009[55], are used as masks to define the geographical boundaries of the ice shelves.

Linear step response model

The extratropical linear response to the precipitation anomaly over the SPCZ box was quantified using the linear response theory method (LRTM), demonstrated by Deb et al.[41]. Using LRTM, the signal *S* at time *t* (days) is expressed as the weighted sum of the lagged forcing *F* for the last *T* days. Mathematically the expression can be written as

$$S(t) = \int_0^T G(\tau) F(t - \tau) d\tau + \epsilon, \qquad (1)$$

where, *G* is the Green's function, which is estimated by the linear least square regression between signal and lagged forcing (ref. [56]). τ represents lag and ϵ is the nonlinear residual term. Here, signal *S* is the 200-hPa geopotential height anomaly over the extratropics of the Southern Hemisphere and forcing *F* is the area-averaged precipitation anomaly over the SPCZ box. Using *G*, the step response at time lag τ_j is calculated using the equation below

$$S_{step}(\tau_j) \approx \sum_{i=0}^{j} G(\tau_i) \Delta\tau. \qquad (2)$$

Here $\Delta\tau$ represents the time interval of the data, which is one day. The quasi-stationary step responses were averaged over a lag of 30–40 days and the averaged response was considered as the extratropical linear response to anomalous precipitation over the SPCZ box.

The extratropical Rossby wave response to anomalous tropical deep convection takes approximately two weeks to evolve into a quasi-stationary pattern[40]. However, temporal variations in the step response persist even after 15 days of the tropical forcing, gradually diminishing after ~30 days[41]. Therefore, a lag of 30–40 days was chosen in the linear step response model to capture the fully developed Rossby wave response.

Determination of waveflux activity

The horizontal component of the wave activity flux associated with the barotropic Rossby wave trains was computed following Karoly et al.[44] as:

$$F_S = \left(F_\lambda, F_\phi\right) = \sigma \cos\phi \left(v'^2 - \frac{1}{2\Omega a \sin 2\phi}\frac{\partial}{\partial\lambda}(v'\Phi'), -u'v' + \frac{1}{2\Omega a \sin 2\phi}\frac{\partial}{\partial\lambda}(u'\Phi')\right)$$

$$(3)$$

where, σ = pressure/1000 hPa, (λ, ϕ) represent longitude and latitude respectively, (u',v') represent the anomalous horizontal geostrophic velocity components derived from the geopotential height anomaly (Φ') of the step response map, Ω represents earth's rotation rate and *a* represents the radius of the earth.

Calculation of Rossby wave source

The Rossby wave source (RWS) was computed following Qin and Robinson[46] as:

$$S' \approx -V_\chi' \cdot \nabla\bar\zeta - \bar\zeta\nabla\cdot V_\chi' \qquad (4)$$

where, V_χ is the divergent (irrotational) component of the wind at 200-hPa, ζ represents absolute vorticity, and *S* is the RWS. The overbar indicates time-mean, and the prime indicates anomaly from time-mean. The first term on

the right-hand side indicates advection of the mean absolute vorticity by the divergent flow anomaly, and the second term is the vortex stretching term. The divergent component of the wind was computed using the "wind-spharm" library[57].

Other atmospheric and oceanic datasets

We use monthly-mean fields of geopotential height at 500 hPa and meridional wind component at 850 hPa from the European Centre for Medium-Range Weather Forecasts (ECMWF) fifth generation atmospheric reanalysis ERA5[58], and the monthly-mean precipitation data from NOAA Climate Prediction Center Merged Analysis of Precipitation (CMAP)[59], for the austral summer months (i.e., December, January, and February). For the Linear response theory model, daily geopotential height was taken from ERA5[58], while the daily precipitation data was taken from the CMAP pentad precipitation dataset. The pentad CMAP data was linearly interpolated to obtain the daily values. The daily anomalies were computed relative to the 1979–2018 mean, following the methodology used in Deb et al.[41]. The datasets were detrended to remove the effect of anthropogenic forcing, retaining interannual variability. Monthly mean SST data during the austral summer months (i.e., December, January, and February) were obtained from the NOAA Extended Reconstructed Sea Surface Temperature V5 dataset[60] available on a $2° \times 2°$ grid.

Data availability

ERA5 dataset is available at: https://cds.climate.copernicus.eu/datasets. NOAA Extended Reconstructed Sea Surface Temperature V5 dataset is available at: https://climatedataguide.ucar.edu/climate-data/sst-data-noaa-extended-reconstruction-ssts-version-5-ersstv5. CMAP precipitation can be downloaded from: https://climatedataguide.ucar.edu/climate-data/cmap-cpc-merged-analysis-precipitation. The surface melt data can be retrieved from: https://snow.univ-grenoble-alpes.fr/melting/. Summer near-surface temperatures from the MetUM simulations used to compute the "melt potential" metrics are available here: https://doi.org/10.5285/05f8bd4b-97b1-43d0-a1c6-66aea7021aaf.

Code availability

Computer codes used for the analysis described in this study can be obtained from the corresponding author on reasonable request.

References

1. Kingslake, J. et al. Widespread movement of meltwater onto and across Antarctic ice shelves. *Nature* **544**, 349–352 (2017).
2. Johnson, A., Hock, R. & Fahnestock, M. Spatial variability and regional trends of Antarctic ice shelf surface melt duration over 1979–2020 derived from passive microwave data. *J. Glaciol.* **68**, 533–546 (2022).
3. Orr, A. et al. Characteristics of surface "melt potential" over Antarctic ice shelves based on regional atmospheric model simulations of summer air temperature extremes from 1979/80 to 2018/19. *J. Clim.* **36**, 3357–3383 (2023).
4. Scambos, T. A. et al. The link between climate warming and break-up of ice shelves in the Antarctic Peninsula. *J. Glaciol.* **46**, 516–530 (2000).
5. MacAyeal, D. R. et al. Catastrophic ice-shelf break-up by an ice-shelf-fragment-capsize mechanism. *J. Glaciol.* **49**, 22–36 (2003).
6. Banwell, A. F., MacAyeal, D. R. & Sergienko, O. V. Breakup of the Larsen B Ice Shelf triggered by chain reaction drainage of supraglacial lakes. *Geophys. Res. Lett.* **40**, 5872–5876 (2013).
7. Banwell, A. F. & MacAyeal, D. R. Ice-shelf fracture due to viscoelastic flexure stress induced by fill/drain cycles of supraglacial lakes. *Antarct. Sci.* **27**, 587–597 (2015).

8. Banwell, A. F. et al. Direct measurements of ice-shelf flexure caused by surface meltwater ponding and drainage. *Nat. Commun.* **10**, 730 (2019).
9. Lai, C.-Y. et al. Vulnerability of Antarctica's ice shelves to meltwater-driven fracture. *Nature* **584**, 574–578 (2020).
10. Pritchard, H. et al. Antarctic ice-sheet loss driven by basal melting of ice shelves. *Nature* **484**, 502–505 (2012).
11. Glasser, N. F. et al. From ice-shelf tributary to tidewater glacier: continued rapid recession, acceleration and thinning of Röhss Glacier following the 1995 collapse of the Prince Gustav Ice Shelf, Antarctic Peninsula. *J. Glaciol.* **57**, 397–406 (2011).
12. Davies, B. J., Carrivick, J. L., Glasser, N. F., Hambrey, M. J. & Smellie, J. L. Variable glacier response to atmospheric warming, northern Antarctic Peninsula, 1988–2009. *Cryosphere* **6**, 1031–1048 (2012).
13. Rignot, E. et al. Four decades of Antarctic ice sheet mass balance from 1979–2017. *Proc. Natl. Acad. Sci. USA* **116**, 1095–1103 (2019).
14. Trusel, L. D. et al. Divergent trajectories of Antarctic surface melt under two twenty-first-century climate scenarios. *Nat. Geosci.* **8**, 927–932 (2015).
15. Gilbert, E. & Kittel, C. Surface melt and runoff on Antarctic ice shelves at 1.5 C, 2 C, and 4 C of future warming. *Geophys. Res. Lett.* **48**, e2020GL091733 (2021).
16. DeConto, R. M. et al. The Paris Climate Agreement and future sea-level rise from Antarctica. *Nature* **593**, 83–89 (2021).
17. DeConto, R. M. & Pollard, D. Contribution of Antarctica to past and future sea-level rise. *Nature* **531**, 591–597 (2016).
18. Vihma, T., Tuovinen, E. & Savijärvi, H. Interaction of katabatic winds and near-surface temperatures in the Antarctic. *J. Geophys. Res. Atmos.* **116**, D21119 (2011).
19. Trusel, L. D. et al. Satellite-based estimates of Antarctic surface meltwater fluxes. *Geophys. Res. Lett.* **40**, 6148–6153 (2013).
20. Nicolas, J. P. et al. January 2016 extensive summer melt in West Antarctica favoured by strong El Niño. *Nat. Commun.* **8**, 15799 (2017).
21. Clem, K. R., Orr, A. & Pope, J. O. The springtime influence of natural tropical Pacific variability on the surface climate of the Ross ice shelf, West Antarctica: implications for ice shelf thinning. *Sci. Rep.* **8**, 1–10 (2018).
22. Deb, P. et al. Summer drivers of atmospheric variability affecting ice shelf thinning in the Amundsen Sea Embayment, West Antarctica. *Geophys. Res. Lett.* **45**, 4124–4133 (2018).
23. Scott, R. C., Nicolas, J. P., Bromwich, D. H., Norris, J. R. & Lubin, D. Meteorological drivers and large-scale climate forcing of West Antarctic surface melt. *J. Clim.* **32**, 665–684 (2019).
24. Chittella, S. P. S., Deb, P. & van Wessem, J. M. Relative contribution of atmospheric drivers to "extreme" snowfall over the Amundsen Sea Embayment. *Geophys. Res. Lett.* **49**, e2022GL098661 (2022).
25. Paolo, F. S. et al. Response of Pacific-sector Antarctic ice shelves to the El Niño/Southern oscillation. *Nat. Geosci.* **11**, 121–126 (2018).
26. Li, X. et al. Impacts of the north and tropical Atlantic Ocean on the Antarctic Peninsula and sea ice. *Nature* **505**, 538–542 (2014).
27. Clem, K. R. & Fogt, R. L. South Pacific circulation changes and their connection to the tropics and regional Antarctic warming in austral spring, 1979–2012. *J. Geophys. Res. Atmos.* **120**, 2773–2792 (2015).
28. Meehl, G. A. et al. Antarctic sea-ice expansion between 2000 and 2014 driven by tropical Pacific decadal climate variability. *Nat. Geosci.* **9**, 590–595 (2016).
29. Li, X. et al. Tropical teleconnection impacts on Antarctic climate changes. *Nat. Rev. Earth Environ.* **2**, 680–698 (2021).
30. Purich, A. et al. Tropical Pacific SST drivers of recent Antarctic sea ice trends. *J. Clim.* **29**, 8931–8948 (2016).
31. Turner, J. et al. Absence of 21st century warming on Antarctic Peninsula consistent with natural variability. *Nature* **535**, 411–415 (2016).

32. Clem, K. R. et al. Role of the South Pacific convergence zone in West Antarctic decadal climate variability. *Geophys. Res. Lett.* **46**, 6900–6909 (2019).

33. Fogt, R. L., Bromwich, D. H. & Hines, K. M. Understanding the SAM influence on the South Pacific ENSO teleconnection. *Clim. Dyn.* **36**, 1555–1576 (2011).

34. Turner, J. et al. The Amundsen sea low. *Int. J. Climatol.* **33**, 1818–1829 (2013).

35. Clem, K. R., Renwick, J. A. & McGregor, J. Large-scale forcing of the Amundsen Sea low and its influence on sea ice and West Antarctic temperature. *J. Clim.* **30**, 8405–8424 (2017).

36. Connolley, W. Variability in annual mean circulation in southern high latitudes. *Clim. Dyn.* **13**, 745–756 (1997).

37. Wille, J. D. et al. Antarctic atmospheric river climatology and precipitation impacts. *J. Geophys. Res. Atmos.* **126**, e2020JD033788 (2021).

38. Wille, J. D. et al. West Antarctic surface melt triggered by atmospheric rivers. *Nat. Geosci.* **12**, 911–916 (2019).

39. Folland, C. K. et al. Relative influences of the interdecadal Pacific oscillation and ENSO on the South Pacific convergence zone. *Geophys. Res. Lett.* **29**, 21–21 (2002).

40. Hoskins, B. J. & Ambrizzi, T. Rossby wave propagation on a realistic longitudinally varying flow. *J. Atmos. Sci.* **50**, 1661–1671 (1993).

41. Deb, P. et al. The extratropical linear step response to tropical precipitation anomalies and its use in constraining projected circulation changes under climate warming. *J. Clim.* **33**, 7217–7231 (2020).

42. Senapati, B. et al. Origin and dynamics of global atmospheric wavenumber-4 in the Southern mid-latitude during austral summer. *Clim. Dyn.* **59**, 1309–1322 (2022).

43. Sen, A., Deb, P., Matthews, A. J. & Joshi, M. M. Teleconnection and the Antarctic response to the Indian Ocean Dipole in CMIP5 and CMIP6 models. *Q. J. R. Meteorol. Soc.* **150**, 5020–5036 (2024).

44. Karoly, D. J., Plumb, R. A. & Ting, M. Examples of the horizontal propagation of quasi-stationary waves. *J. Atmos. Sci.* **46**, 2802–2811 (1989).

45. Sardeshmukh, P. D. & Hoskins, B. J. The generation of global rotational flow by steady idealized tropical divergence. *J. Atmos. Sci.* **45**, 1228–1251 (1988).

46. Qin, J. & Robinson, W. A. On the Rossby wave source and the steady linear response to tropical forcing. *J. Atmos. Sci.* **50**, 1819–1823 (1993).

47. Fogt, R. L. et al. Historical SAM variability. Part II: twentieth-century variability and trends from reconstructions, observations, and the IPCC AR4 models. *J. Clim.* **22**, 5346–5365 (2009).

48. Jones, M. E. et al. Sixty years of widespread warming in the southern middle and high latitudes (1957–2016). *J. Clim.* **32**, 6875–6898 (2019).

49. Thompson, D. W. J. & Solomon, S. Interpretation of recent Southern Hemisphere climate change. *Science* **296**, 895–899 (2002).

50. Mayewski, P. A. et al. State of the Antarctic and Southern Ocean climate system. *Rev. Geophys.* **47**, https://doi.org/10.1029/2007RG000231 (2009).

51. Thompson, D. W. J. et al. Signatures of the Antarctic ozone hole in Southern Hemisphere surface climate change. *Nat. Geosci.* **4**, 741–749 (2011).

52. Torinesi, O., Fily, M. & Genthon, C. Variability and trends of the summer melt period of Antarctic ice margins since 1980 from microwave sensors. *J. Clim.* **16**, 1047–1060 (2003).

53. Picard, G. & Fily, M. Surface melting observations in Antarctica by microwave radiometers: correcting 26-year time series from changes in acquisition hours. *Remote Sens. Environ.* **104**, 325–336 (2006).

54. Mann, H. B. Nonparametric tests against trend. *Econometrica* **13**, 245–259 (1945).

55. Mouginot, J., Rignot, E. & Scheuchl, B. MEaSUREs Antarctic boundaries for IPY 2007-2009 from satellite radar, version 1 [Data Set]. https://doi.org/10.5067/SEVV4MR8P1ZN (2016).

56. Kostov, Y. et al. Fast and slow responses of Southern Ocean sea surface temperature to SAM in coupled climate models. *Clim. Dyn.* **48**, 1595–1609 (2017).

57. Dawson, A. Windspharm: a high-level library for global wind field computations using spherical harmonics. *J. Open Res. Softw.* **4**, e31 (2016).

58. Hersbach, H. et al. The ERA5 global reanalysis. *Q. J. R. Meteorol. Soc.* **146**, 1999–2049 (2020).

59. Xie, P. & Arkin, P. A. Global precipitation: a 17-year monthly analysis based on gauge observations, satellite estimates, and numerical model outputs. *Bull. Am. Meteorol. Soc.* **78**, 2539–2558 (1997).

60. Huang, B. & Coauthors. NOAA extended reconstructed sea surface temperature (ERSST), version 5. NOAA National Centers for Environmental Information. https://doi.org/10.7289/V5T72FNM (2017b).

Author contributions

P.D. conceived the study, analyzed the results, and led the writing of the manuscript. D.B. and A.O. contributed to the conceptualization, analysis, and writing of the manuscript. A.S. and K.R.C. assisted with the analysis of results and the writing of the manuscript.

Competing interests

The authors declare no competing interests.

Additional information

Supplementary information The online version contains supplementary material available at https://doi.org/10.1038/s43247-025-02077-8.

Correspondence and requests for materials should be addressed to Pranab Deb.

Peer review information *Communications Earth & Environment* thanks Rebecca Baiman and the other, anonymous, reviewer(s) for their contribution to the peer review of this work. Primary Handling Editor: Alireza Bahadori. A peer review file is available.

Reprints and permissions information is available at http://www.nature.com/reprints